# The Ionic Kerr Effect

M. Basini[†],[1] M. Udina[†,*],[2] M. Pancaldi,[3,4] V. Unikandanunni,[1] S. Bonetti,[1,3] and L. Benfatto[2]

[1] *Department of Physics, Stockholm University, 10691 Stockholm, Sweden*

[2] *Department of Physics and ISC-CNR, "Sapienza" University of Rome, P.le A. Moro 5, 00185 Rome, Italy*

[3] *Department of Molecular Sciences and Nanosystems, Ca' Foscari University of Venice, 30172 Venice, Italy*

[4] *Elettra-Sincrotrone Trieste S.C.p.A., 34149 Basovizza, Trieste, Italy*

(Dated: January 16, 2023)

## Abstract

The Kerr effect measures a change in the refractive index proportional to the intensity of the applied electric field, and its ultrafast implementation has been widely used to investigate the nonlinear optical properties of many different systems. More recently, the same mechanism has been exploited with terahertz light pulses to access resonant processes involving lattice vibrations or broken-symmetry collective modes. Here we provide experimental evidence and theoretical description that in insulating $SrTiO_3$ the terahertz Kerr effect admits a sizeable response due to lattice degrees of freedom. This ionic contribution exploits the ability of strong terahertz pulses to excite multiple infrared phonons at an intermediate step before or after the usual off-resonant electronic excitations responsible for the electronic Kerr effect. The mechanism is identified thanks to a quantitative theoretical model of the time and polarization dependence of both the electronic and phononic responses. Such a ionic Kerr effect provides a tunable mechanism to modulate the refractive index on ultrashort time-scales and, given the capability of terahertz-driven phonons to couple to order parameters and to drive materials towards metastable states which may not be accessible at thermal equilibrium, it can be used to investigate the electron-phonon coupling across various phase transitions.

† These authors contributed equally to this work

∗ mattia.udina@uniroma1.it

The latest advances in the generation of intense terahertz (THz) field pulses have allowed to investigate the low-frequency counterpart of nonlinear optical phenomena in condensed matter, conventionally studied with visible light, as it is the case for the THz Kerr effect[1–3]. Broadly, the Kerr effect measures a change in the refractive index proportional to the intensity of the applied electric field, and it is a standard manifestation of the non-linear optical properties of the medium[4]. When THz pump pulses are applied, the signal can be strongly enhanced by matching low-lying excitations in the same frequency range, such as lattice vibrations[5,6], or collective-modes in broken-symmetry states, as for magnetic[7–11] or superconducting transitions[12–14]. Such a resonant response usually adds up to the background response of electrons, and it can be used to identify the microscopic mechanisms underlying the coupling among different degrees of freedom. This is the case of experiments in the regime of non-linear phononics, where one exploits the ability of infrared-active vibrational modes, driven by strong THz pulses, to anharmonically couple to other phononic excitations[15–19]. This approach has the potential to open a pathway to drive materials towards metastable states which may not be accessible at thermal equilibrium[20].

In order to drive a material in the non-linear phononics regime, large amplitude phonon displacements need to be achieved. The archetypal perovskite $SrTiO_3$ (STO) is a quantum paraelectric[21] showing a large dielectric constant at room temperature ($\epsilon_0 \approx 300$), and with a low-lying phonon mode that progressively soften as the temperature is lowered[22–24]. Such excitation is an infrared-active (IR-active) transverse optical ($TO_1$) phonon, and it is the same phonon mode which is responsible for the paraelectric to ferroelectric transition upon, e.g., Ca doping[25]. Furthermore, it has been recently pointed out its possible role in the superconducting transition in electron-doped samples[26–28], and the possibility of realizing dynamical multiferrocity upon driving with circularly polarized THz electric fields[29,30]. Similarly to STO, other perovskite materials such as $KTaO_3$ host a soft $TO_1$ phonon mode that has been suggested to be relevant for the magnetic[31,32] and superconducting[33] response.

In this work, we demonstrate the presence in cubic STO of a ionic contribution to the THz Kerr response, which we name ionic Kerr effect (IKE). In fact, besides the well-studied electronic Kerr effect (EKE), due to off-resonant electronic transitions in wide-band insulating STO[34], the IKE can be associated with the non-linear excitation of the $TO_1$ mode, see Fig. 1. We show that the excitation of the IR active $TO_1$ phonon mode by a THz field

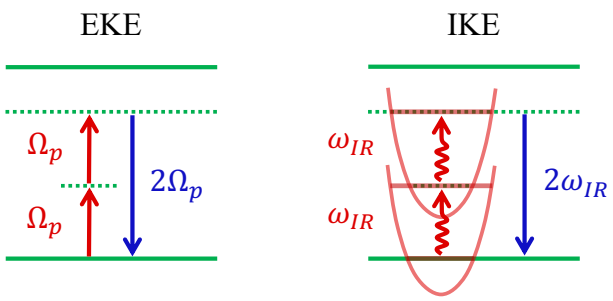


Figure 1. **Terahertz electronic and ionic Kerr effect in a wide-band insulator.** In the THz EKE (left panel) the relevant electronic transition is driven by a sum-frequency two-photons Raman-like process. In an insulator the intermediate electronic state (dashed line) is virtual, so it relaxes back almost instantaneously giving a $2\Omega_p$ modulation of the emitted light. In the THz IKE (right panel) two IR-active phonons can be used to reach the virtual electronic state (process labeled as (a) in the text), leading to a modulation at $2\phi_{IR}$. This pathway only occurs when the THz pulse is resonantly tuned to the phonon frequency, i.e. when $\phi_{IR} \simeq \emptyset_p$.

pulse manifests itself with a sizable temperature dependence of the Kerr response, which is unexpected for the EKE in a wide-band insulator. In contrast, the IKE rapidly disappears by decreasing temperature, due to the phonon frequency softening far below the central frequency of the pump field. We are able to clearly distinguish between EKE and IKE thanks to a detailed theoretical description of the THz Kerr signal, which we retrieve experimentally as a function of the light polarization and of the pump-probe time delay $t_{pp}$.

**Balanced detection of the THz Kerr response.** Measurements are performed on a 500 $\mu$m-thick $SrTiO_3$ crystal substrate (MTI Corporation), cut with the [001] crystallographic direction out of plane. Broadband single-cycle terahertz radiation is generated in a DSTMS crystal via optical rectification of a 40 fs-long, 800 $\mu$J near-infrared laser pulse centered at a wavelength of 1300 nm. The near-infrared pulse is obtained by optical parametric amplification from a 40 fs-long, 6.3 mJ pulse at 800 nm wavelength, produced by a 1 kHz regenerative amplifier. As schematically shown in Fig. 2, the broadband terahertz pulses are filtered with a 3 THz band-pass filter, resulting in a peak frequency of $\emptyset_p/2\pi = 3$ THz (with peak amplitude of 330 kV/cm), and focused onto the sample to a spot of approximately 500 $\mu$m in diameter. The time-delayed probe beam, whose polarization is controlled by means of a nanoparticle linear film polarizer, is a 40 fs-long pulse at 800 nm wavelength nor-

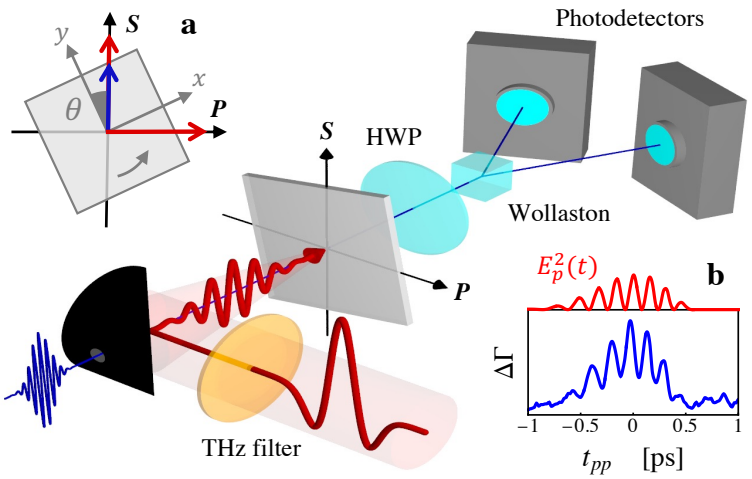


Figure 2. **Schematics of the experimental setup.** The THz pulse is in red while the optical probe is in blue. Inset **a**: schematic of the polarization geometry. The sample is rotated in the $(S, P)$ plane, such that the $y$ crystallographic direction forms a variable angle $\theta$ with respect to $S$. The probe (blue arrow) polarization is fixed along $S$, while the pump pulse (red arrow) is polarized along either $S$ or $P$ for linearly polarized light and in both directions for circularly polarized light. Inset **b**: typical time-trace of $\Delta\Gamma$ at fixed $\theta = 67.5°$ (blue line) compared with the intensity profile of the linear pump pulse (red line).

mally incident onto the sample surface. A 100 $\mu$m-thick BBO crystal ($\beta$-$BaB_2O_4$, Newlight Photonics) and a shortpass filter are used for converting the probe wavelength to 400 nm and increasing the signal-to-noise ratio in temperature-dependent measurements. The probe size at the sample is approximately 100 $\mu$m, substantially smaller than the THz pump. The half-wave plate (HWP) located after the sample is used to detect the polarization rotation of the incoming field induced by the non-linear response, and a Wollaston prism is used to implement a balanced detection scheme with two photodiodes. The signals from the photodiodes are fed to a lock-in amplifier, whose reference frequency (500 Hz) comes from a chopper mounted in the pump path before the DSTMS crystal.

Data are collected as a function of the $t_{pp}$ time-delay as well as a function of the angle $\theta$ that the probe polarization direction forms with respect to the main crystallographic axes. For convenience, the probe beam is kept fixed along the $S$ direction, such that $\mathbf{E}_{pr}(t) = (E_{pr}(t)\sin\theta, E_{pr}(t)\cos\theta)$, while the pump field $\mathbf{E}_p$ can be either linearly polarized (along $S$ or $P$ direction) or circularly polarized[29], by placing a quarter-wave plate after the band-pass

filter, such that in general

$$\mathbf{E}_p(t) = \begin{pmatrix} E_{p,S}(t)\sin\theta + E_{p,P}(t)\cos\theta \\ E_{p,S}(t)\cos\theta - E_{p,P}(t)\sin\theta \end{pmatrix}. \tag{1}$$

In the presence of Kerr rotation the probe field transmitted through the sample $\tilde{\mathbf{E}}(t)$ acquires in general a finite $P$ component. The half-wave plate rotates $\tilde{\mathbf{E}}(t)$ by 45° with respect to the $P$ direction, so the outgoing signal reaching the two photodetectors $(\Gamma_1, \Gamma_2)$ reads[35]

$$\begin{pmatrix} \Gamma_1 \\ \Gamma_2 \end{pmatrix} \propto \begin{pmatrix} 1 & 1 \\ 1 & -1 \end{pmatrix} \begin{pmatrix} \tilde{E}_S \\ \tilde{E}_P \end{pmatrix}. \tag{2}$$

In a pump-probe detection scheme, the use of a chopper on the pump path allows for measuring, with a lock-in amplifier, the differential intensity $|\Gamma_1|^2 - |\Gamma_2|^2$ with (*on*) and without (*off*) the pump, to obtain

$$\Delta\Gamma = \Delta\Gamma_{on} - \Delta\Gamma_{off} \propto (\tilde{E}_S\tilde{E}_P)_{on} - (\tilde{E}_S\tilde{E}_P)_{off}. \tag{3}$$

A typical time-trace of $\Delta\Gamma$ for a linearly polarized pump pulse along $P$ and at fixed angle $\theta$ is shown in Fig. 2**b**, together with $E_p^2(t)$. As we shall see below, the close qualitative correspondence among the two signals is a direct consequence of pumping a band insulator much below the band gap. To measure the angular dependence of the response, we then choose $t_{pp}$ at the maximum $\Delta\Gamma$ amplitude, and we record its change as a function of $\theta$. The results are shown in Fig. 3**a** for both linearly polarized (in either $SS$ or $SP$ configuration, where first letter describes the probe polarization, while the second letter states the pump polarization) or circularly polarized pump pulses. In all cases, the signal displays a marked four-fold angular dependency, along with a smaller two-fold periodicity.

**Off-resonant electronic Kerr effect.** In order to assess such angular dependence, we first outline the theoretical description of the conventional EKE, as it emerges out of Eq. (3). The transmitted probe field $\tilde{\mathbf{E}}(t)$ will contain both linear and non-linear components with respect to the total applied field $\mathbf{E}_p + \mathbf{E}_{pr}$. Since the detection is restricted around the frequency range of the visible probe field, the linear response to the pump can be discarded, as well as higher-harmonics of the probe generated inside the sample. We can then retain for $\tilde{E}_S \sim P_S^{(1)}$, with $P_S^{(1)}$ the linear response to the probe along $S$, while $\tilde{E}_P$ scales as the third-order polarization for a centro-symmetric system, i.e. $\tilde{E}_P \sim P_P^{(3)}$. By decomposing

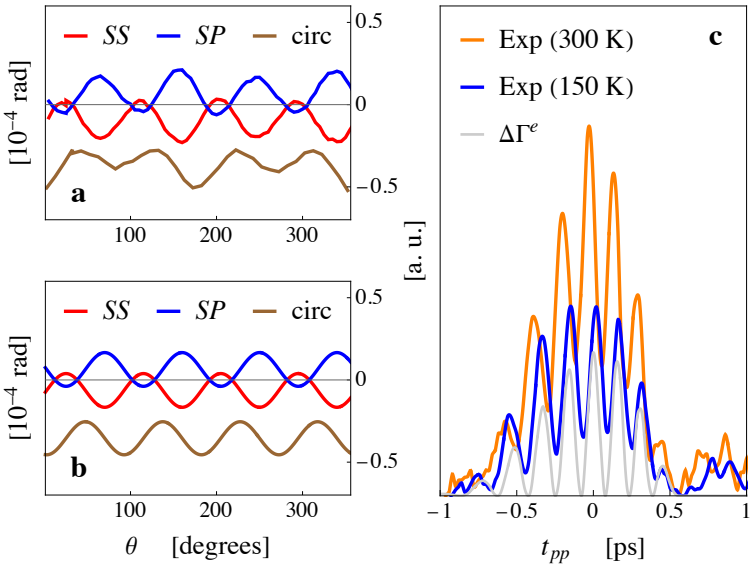


Figure 3. **Polarization and time dependence of the THz Kerr effect.** **a** Experimental data as a function of $\theta$ at fixed time-delay $t^*_{pp}$ in the parallel $SS$ (red curve), cross-polarized $SP$ (blue curve) and circular (brown curve) configuration. **b** Corresponding simulations from Eq. (6), accounting for a small polarization misalignment ($\Delta_\theta = 5°$) between the pump and probe pulses. **c** Experimental data as a function of $t_{pp}$ at fixed angle $\theta = 67.5°$ in the $SP$ configuration at 300 K (orange curve) and 150 K (blue curve), compared with the simulated off-resonant electronic contribution $\Delta\Gamma^e$ (gray curve).

$P_P^{(3)}$ in its $(x, y)$ components one gets:

$$\Delta\Gamma \propto \tilde{E}_S P_P^{(3)} = \tilde{E}_S \left[\cos\theta P_x^{(3)} - \sin\theta P_y^{(3)}\right]. \tag{4}$$

As mentioned above only contributions linear in $E_{pr}$ to $P_P^{(3)} \simeq \chi^{(3)} E_{pr} E_p^2$ must be retained, where $\chi^{(3)}$ is the third-order susceptibility tensor. By making explicit the space and time dependence one can finally write:

$$P_i^{(3)}(t, t_{pp}) = \int dt' \sum_{jkl} E_{pr,j}(t) \chi^{(3)}_{ijkl}(t + t_{pp} - t') \bar{E}_{p,k}(t') \bar{E}_{p,l}(t'), \tag{5}$$

where we introduced the time shift $t_{pp}$ between the pump and probe pulses, such that $\bar{E}_p(t + t_{pp}) \equiv E_p(t)$, with $\bar{E}_p(t)$ and $E_{pr}(t)$ centered around $t = 0$ (see Refs.[36,37] for a similar approach). Since the pump frequency is much smaller than the electronic band gap ($\sim 3$ eV), the nonlinear electronic response should be ascribed to off-resonant interband excitations, leading to a nearly instantaneous contribution to the third-order susceptibility tensor $\chi^{(3)}$,

which can be well approximated by a Dirac delta-function, i.e. $\chi^{(3)}_{ijkl}(t) \sim \chi^{(3)}_{ijkl}\delta(t)$, with $\chi^{(3)}_{ijkl}$ a constant value. Under this assumption, Kleinman symmetry for the cubic $m3m$ class appropriate for STO above $T_s$ assures that the off-diagonal components of the third-order susceptibility tensor have the same magnitude[4]. In the specific case of insulating $SrTiO_3$, at room temperature one finds $\chi^{(3)}_{iijj} = \chi^{(3)}_{ijji} = \chi^{(3)}_{ijij} \simeq 0.47\chi^{(3)}_{iiii}$[38]. Finally, since the measurement at the photodetectors corresponds to the time-average field intensity $|\Gamma_i|^2$, one can replace $E_{pr,j}(t)$ in Eq. (5) with its value at $t = 0$, so that the probe pulse acts as an overall prefactor, relevant only for its polarization dependence. With straightforward algebra, and using the decomposition (1) and (4), one obtains the general expression for the EKE:

$$\Delta\Gamma^e(t_{pp},\theta) \propto \frac{1}{4}E_{pr}(0)\Big[\bar{E}^2_{p,P}(t_{pp}) - \bar{E}^2_{p,S}(t_{pp})\Big]\left(\chi^{(3)}_{xxxx} - 3\chi^{(3)}_{xxyy}\right)\sin(4\theta) + \\ + 2E_{pr}(0)\bar{E}_{p,P}(t_{pp})\bar{E}_{p,S}(t_{pp})\Big[\chi^{(3)}_{xxyy} + \frac{1}{2}\left(\chi^{(3)}_{xxxx} - 3\chi^{(3)}_{xxyy}\right)\sin^2(2\theta)\Big]. \qquad (6)$$

For linearly polarized pump in the $SS$ configuration $\bar{E}_{p,P} = 0$. Thus choosing a fixed $t^*_{pp}$ where $\bar{E}_{p,S}(t^*_{pp})$ is maximized one has:

$$\Delta\Gamma^e(t^*_{pp},\theta) \propto -(\chi^{(3)}_{xxxx} - 3\chi^{(3)}_{xxyy})\bar{E}^2_{p,S}(t^*_{pp})\sin(4\theta), \qquad (7)$$

leading to the four-fold symmetric signal shown in Fig. 3**b**. As anticipated, the general scaling in $t_{pp}$ as $E^2_p(t_{pp})$ is a consequence of exciting electronic transitions below the band gap, leading to an instantaneous relaxation ($\chi^{(3)} \sim \delta(t)$) of the intermediate state, detected as a small $2\Omega_p$ modulation of the probe pulse. Eq. (6) accounts very well for the angular dependence reported in Fig. 3**a**. Within the same formalism, a small polarization misalignment $\Delta_\theta$ between the pump and probe pulses with respect to $S$ has been considered to explain the small overall (positive or negative) shift of the signal (labeled $SS$) in Fig. 3**a**, around which the oscillations occur (see Supplementary Material). In the cross-polarized $SP$ configuration, where the linear pump lies along the $P$ direction ($\bar{E}_{p,S} = 0$), Eq. (6) predicts an overall sign change in the measured quantity, as indeed observed experimentally, see Fig. 3**a** ($SP$ line). When instead circularly polarized pulses are applied, the mixed term $\bar{E}_{p,P}\bar{E}_{p,S}$ in Eq. (6) is different from zero and carries a finite isotropic contribution leading to a sizable vertical shift of the signal (even if $\Delta_\theta = 0$), which has been also observed, see line *circ* in Fig. 3**a**. Notice that the difference signal between right-handed and left-handed circularly polarized light, as the one measured in Ref.[29], picks up only the $E_{p,P}E_{p,S}$ term of Eq. (6), since a helicity change corresponds to a sign change for one of the two components.

Beside the expected 4-fold symmetric contribution encoded in Eq. (6), we detect a subleading 2-fold symmetric contribution, which can be ascribed to residual detection effects not included in the present modelling. Finally, we observe that Eq. (7) closely resembles the polarization and directional dependence of the specular nonlinear anisotropic polarization effect (SNAPE), already reported in cubic crystals for linearly polarized optical pump pulses in the $SS$ configuration[39,40].

Despite the excellent agreement between the theoretical expression (6) and the measured angular dependence of the signal, marked deviations are observed for the temperature dependence of the signal. Fig. 3**c** shows the time-dependent traces in the $SP$ configuration at fixed angle $\theta$ and two different temperatures. In particular, due to the large value of the band gap, it is hard to ascribe the significant temperature variations observed experimentally to an analogous temperature dependence of the electronic $\chi^{(3)}$ tensor. In addition, besides the oscillating component at $\sim 2\emptyset_p$, which is consistent with Eq. (6) following the squared pump field in time, a non-oscillating underlying background is found.

**Resonant ionic Kerr effect.** Here we argue that, besides the EKE, the non-linear response behind the THz Kerr effect admits an intermediate process that we name IKE, where the virtual electronic state is reached via (or decays to) an intermediate two-phonon excitation triggered by two photons of the THz pump pulse, see Fig. 1. The frequency of the $TO_1$ IR-active phonon mode softens from 3.2 to 1.8 THz when lowering the temperature from 380 to 150 K in the cubic phase of STO[24,41]. As a consequence, the IKE is maximized at room temperature, where the frequency spectrum of our THz pump pulse overlaps with the phonon mode, while it gets progressively suppressed by the phonon softening below the pump frequency under cooling. As detailed in the Supplementary Material, two intermediate phonon processes are possible. In one case, denoted by $\Delta\Gamma^{ph,(a)}$, the primary excitation consists in two photons driving two phonons with a strength controlled by the phonon effective charge $Z$, and only after a virtual electronic state is reached. This process, sketched in Fig. 1, can be effectively accounted by simply replacing the driving pump field $\bar{E}_{p,P(S)}$ in Eq. (6) with

$$\bar{F}^{(a)}_{P(S)}(t_{pp}) \propto \int dt' D(t') \bar{E}_{p,P(S)}(t_{pp} - t'), \tag{8}$$

where $D(t) \equiv \theta(t) e^{-\gamma_T t} \sin(\omega_T t)$ is the (single) phonon propagator, being $\gamma_T$ and $\omega_T$ the phonon broadening and frequency at temperature $T$. In the second process, denoted by $\Delta\Gamma^{ph,(b)}$, the intermediate electronic state itself delivers its energy to two IR phonons with

opposite momenta, leading to an effective modulation of the $\chi^{(3)}$ tensor. This process can be described by replacing the $\bar{E}_{p,P(S)}\bar{E}_{p,P(S)}$ product in Eq. (6) with

$$\bar{F}^{(b)}_{P(S)P(S)}(t_{pp}) \propto \int dt' P(t_{pp}-t')\bar{E}_{p,P(S)}(t')\bar{E}_{p,P(S)}(t'), \tag{9}$$

where $P(t) \equiv \theta(t)\coth\left(\frac{\hbar\omega_T}{2k_BT}\right)e^{-2\gamma_T t}\sin(2\omega_T t)$ is the two-phonon propagator[42,43]. In both cases, the resulting phonon-mediated contribution to the third-order polarization, leading to the IKE, is quadratic with respect to the pump pulse and linear with respect to the probe field, sharing the same general structure of Eq. (5). The full measured quantity, accounting for both the EKE and IKE, i.e.

$$\Delta\Gamma = \Delta\Gamma^{e} + \Delta\Gamma^{ph,(a)} + \Delta\Gamma^{ph,(b)}, \tag{10}$$

is expected to preserve the same polarization dependence of $\Delta\Gamma^{e}$, but with a different temporal profile, due to the time delay in the intermediate excitation of the IR-active phonons, and a marked $T$ dependence of the IKE. Experimental data and theoretical predictions are compared in Fig. 4**a-b**. As expected, even assuming a temperature-independent strength of the electron-phonon coupling, the IKE, is strongly reduced once the resonant condition between the soft-phonon mode and the pump field is lost, in good agreement with the experimental findings (see Fig. 4**c-d**). The correspondence between time-domain measurements and simulations could be further improved by accounting for dispersion effects, which have been recently discussed within the context of Kerr measurements in thick samples at optical frequencies[37,44]. We leave these considerations to future works.

**Discussion and conclusions.** In the present manuscript we demonstrate a direct contribution of the soft IR active $TO_1$ phonon to the THz Kerr effect in insulating STO. In analogy with previously discussed non-linear phononic effects, the basic mechanism relies on a two-phonon excitation by a strong THz light pulse. However, in the IKE observed here the lattice vibrations do not anharmonically couple to other lattice degrees of freedom but directly couple to off-resonant electronic states, leading to a modulation of the conventional EKE. The identification of the phonon contribution is made possible by a microscopic theoretical description of the temporal and angular dependence of the THz Kerr effect measured via balanced detection. Such a theoretical framework can be further extended to describe phase of different lattice symmetries, opening the avenue for the full exploitation of the IKE to investigate the electron-phonon coupling across various phase transitions. In addition,

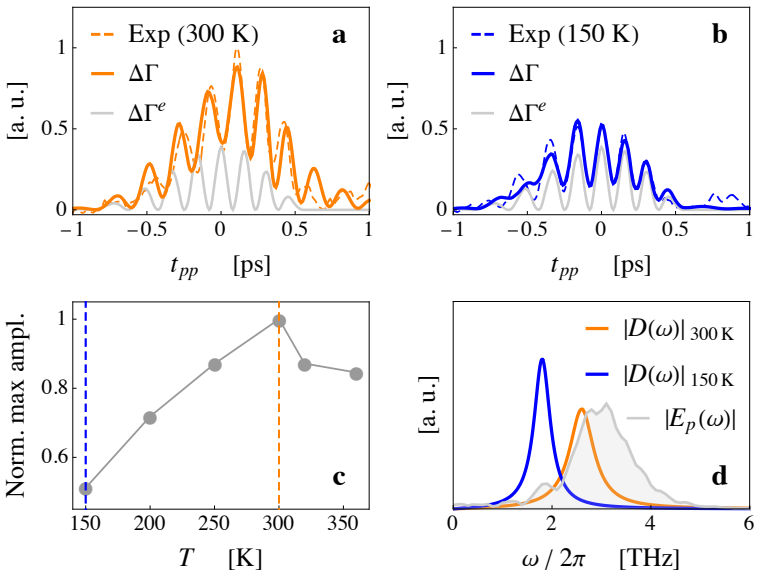


Figure 4. **Ionic contribution to the THz Kerr response. a-b** Comparison between experimental data (dashed lines) and numerical simulations, in the absence (gray solid line) and in the presence of phonon-mediated processes at 300 K (orange solid line) and 150 K (blue solid line). **c** Full temperature evolution of the maximum in $\Delta\Gamma$ normalized to its $T = 300$ K value. **d** Spectral content of the linear pump pulse (gray line) compared to the simulated Fourier transform of the IR-active phonon propagator at 300 K (orange line) and 150 K (blue line). Here we set $(\omega_T, \gamma_T)/2\pi \simeq (2.6, 0.3)$ THz at 300 K and $(\omega_T, \gamma_T)/2\pi \simeq (1.8, 0.2)$ THz at 150 K, in agreement with hyper-Raman measurements[24].

the IKE may provide valuable fingerprints to study the same $TO_1$ soft phonon mode in similar perovskite materials, such as $KTaO_3$, where the associated lattice vibrations in the presence of spin-orbit[45] can play a crucial role in driving the superconducting transition in $KTaO_3$-based heterostructures[33].

**Acknowledgments.** We are thankful to A. Geraldi and M. N. Gastiasoro for fruitful discussions. M. Basini and S. Bonetti acknowledge support from the Knut and Alice Wallenberg Foundation, grants No. 2017.0158 and 2019.0068. M. Udina and L. Benfatto acknowledge financial support by EU under MORE-TEM ERC-SYN (grant agreement No 951215).

**Author contributions.** L.B. and S.B. conceived the problem and supervised the work. M.B., M.P. and S.B. designed the experiment. M.B. and M.P. performed the experiments with the aid of V.U. M.U. and L.B. elaborated the theoretical model and carried out the numerical simulations with input from M.B. and M.P. All authors discussed the results. M.U., M.B. and L.B. wrote the manuscript with input from all authors.

**Competing interests.** The authors declare no competing interests.

---


[1] Mohsen Sajadi, Martin Wolf, and Tobias Kampfrath, "Terahertz-field-induced optical birefringence in common window and substrate materials," Opt. Express **23**, 28985–28992 (2015).

[2] Matthias C. Hoffmann, Nathaniel C. Brandt, Harold Y. Hwang, Ka-Lo Yeh, and Keith A. Nelson, "Terahertz kerr effect," Applied Physics Letters **95**, 231105 (2009), https://doi.org/10.1063/1.3271520.

[3] A. A. Melnikov, V. E. Anikeeva, O. I. Semenova, and S. V. Chekalin, "Terahertz kerr effect in a methylammonium lead bromide perovskite crystal," Phys. Rev. B **105**, 174304 (2022).

[4] Robert W. Boyd, *Nonlinear Optics, Third Edition*, 3rd ed. (Academic Press, Inc., USA, 2008).

[5] Courtney L. Johnson, Brittany E. Knighton, and Jeremy A. Johnson, "Distinguishing nonlinear terahertz excitation pathways with two-dimensional spectroscopy," Phys. Rev. Lett. **122**, 073901 (2019).

[6] C L Korpa, Gy Tóth, and J Hebling, "Mapping the lattice-vibration potential using terahertz pulses," Journal of Physics B: Atomic, Molecular and Optical Physics **51**, 035403 (2018).

[7] Tobias Kampfrath, Alexander Sell, Gregor Klatt, Alexej Pashkin, Sebastian Mährlein, Thomas Dekorsy, Martin Wolf, Manfred Fiebig, Alfred Leitenstorfer, and Rupert Huber, "Coherent terahertz control of antiferromagnetic spin waves," Nature Photonics **5**, 31–34 (2011).

[8] S. Baierl, M. Hohenleutner, T. Kampfrath, A. K. Zvezdin, A. V. Kimel, R. Huber, and R. V. Mikhaylovskiy, "Nonlinear spin control by terahertz-driven anisotropy fields," Nature Photonics **10**, 715–718 (2016).

[9] S. Bonetti, M. C. Hoffmann, M.-J. Sher, Z. Chen, S.-H. Yang, M. G. Samant, S. S. P. Parkin, and H. A. Dürr, "Thz-driven ultrafast spin-lattice scattering in amorphous metallic ferromagnets," Phys. Rev. Lett. **117**, 087205 (2016).

[10] E. A. Mashkovich, K. A. Grishunin, R. V. Mikhaylovskiy, A. K. Zvezdin, R. V. Pisarev, M. B.

Strugatsky, P. C. M. Christianen, Th. Rasing, and A. V. Kimel, "Terahertz optomagnetism: Nonlinear thz excitation of ghz spin waves in antiferromagnetic $febo_3$," Phys. Rev. Lett. **123**, 157202 (2019).

[11] Evgeny A. Mashkovich, Kirill A. Grishunin, Roman M. Dubrovin, Anatoly K. Zvezdin, Roman V. Pisarev, and Alexey V. Kimel, "Terahertz light-driven coupling of antiferromagnetic spins to lattice," Science **374**, 1608–1611 (2021), https://www.science.org/doi/pdf/10.1126/science.abk1121.

[12] Kota Katsumi, Naoto Tsuji, Yuki I. Hamada, Ryusuke Matsunaga, John Schneeloch, Ruidan D. Zhong, Genda D. Gu, Hideo Aoki, Yann Gallais, and Ryo Shimano, "Higgs mode in the $d$-wave superconductor $Bi_2Sr_2CaCu_2O_{8+x}$ driven by an intense terahertz pulse," Phys. Rev. Lett. **120**, 117001 (2018).

[13] Kota Katsumi, Zhi Zhong Li, Hélène Raffy, Yann Gallais, and Ryo Shimano, "Superconducting fluctuations probed by the higgs mode in $Bi_2Sr_2CaCu_2O_{8+x}$ thin films," Phys. Rev. B **102**, 054510 (2020).

[14] R. Grasset, K. Katsumi, P. Massat, H.-H. Wen, X.-H. Chen, Y. Gallais, and R. Shimano, "Terahertz pulse-driven collective mode in the nematic superconducting state of $Ba_{1-x}K_xFe_2As_2$," npj Quantum Materials **7**, 4 (2022).

[15] Dominik M. Juraschek and Sebastian F. Maehrlein, "Sum-frequency ionic raman scattering," Phys. Rev. B **97**, 174302 (2018).

[16] A. von Hoegen, R. Mankowsky, M. Fechner, M. Först, and A. Cavalleri, "Probing the interatomic potential of solids with strong-field nonlinear phononics," Nature **555**, 79–82 (2018).

[17] M. Först, C. Manzoni, S. Kaiser, Y. Tomioka, Y. Tokura, R. Merlin, and A. Cavalleri, "Nonlinear phononics as an ultrafast route to lattice control," Nature Physics **7**, 854–856 (2011).

[18] Alaska Subedi, Andrea Cavalleri, and Antoine Georges, "Theory of nonlinear phononics for coherent light control of solids," Phys. Rev. B **89**, 220301 (2014).

[19] Xian Li, Tian Qiu, Jiahao Zhang, Edoardo Baldini, Jian Lu, Andrew M. Rappe, and Keith A. Nelson, "Terahertz field-induced ferroelectricity in quantum paraelectric $SrTiO_3$," Science **364**, 1079–1082 (2019), https://www.science.org/doi/pdf/10.1126/science.aaw4913.

[20] Ankit S. Disa, Tobia F. Nova, and Andrea Cavalleri, "Engineering crystal structures with light," Nature Physics **17**, 1087–1092 (2021).

[21] S. E. Rowley, L. J. Spalek, R. P. Smith, M. P. M. Dean, M. Itoh, J. F. Scott, G. G. Lonzarich,

and S. S. Saxena, "Ferroelectric quantum criticality," Nature Physics **10**, 367–372 (2014).

[22] M. Kozina, M. Fechner, P. Marsik, T. Van Driel, J. M. Glownia, C. Bernhard, M. Radovic, D. Zhu, S. Bonetti, U. Staub, and M. C. Hoffmann, "Terahertz-driven phonon upconversion in $SrTiO_3$," Nature Physics **15**, 387–392 (2019).

[23] P. Marsik, K. Sen, J. Khmaladze, M. Yazdi-Rizi, B. P. P. Mallett, and C. Bernhard, "Terahertz ellipsometry study of the soft mode behavior in ultrathin $SrTiO_3$ films," Applied Physics Letters **108**, 052901 (2016), https://doi.org/10.1063/1.4940976.

[24] H. Vogt, "Refined treatment of the model of linearly coupled anharmonic oscillators and its application to the temperature dependence of the zone-center soft-mode frequencies of $KTaO_3$ and $SrTiO_3$," Phys. Rev. B **51**, 8046–8059 (1995).

[25] Carl Willem Rischau, Xiao Lin, Christoph P. Grams, Dennis Finck, Steffen Harms, Johannes Engelmayer, Thomas Lorenz, Yann Gallais, Benoît Fauqué, Joachim Hemberger, and Kamran Behnia, "A ferroelectric quantum phase transition inside the superconducting dome of $Sr_{1-x}Ca_xTiO_{3-\delta}$," Nature Physics **13**, 643–648 (2017).

[26] Jonathan M. Edge, Yaron Kedem, Ulrich Aschauer, Nicola A. Spaldin, and Alexander V. Balatsky, "Quantum critical origin of the superconducting dome in $srtio_3$," Phys. Rev. Lett. **115**, 247002 (2015).

[27] Maria N. Gastiasoro, Jonathan Ruhman, and Rafael M. Fernandes, "Superconductivity in dilute $SrTiO_3$: A review," Annals of Physics **417**, 168107 (2020), eliashberg theory at 60: Strong-coupling superconductivity and beyond.

[28] Maria N. Gastiasoro, M. E. Temperini, P. Barone, and J. Lorenzana, Generalized Rashba Electron-Phonon Coupling and Superconductivity in Strontium Titanate. Preprint at https://arxiv.org/abs/2210.05753 (2022).

[29] M. Basini, M. Pancaldi, B. Wehinger, M. Udina, T. Tadano, M. Hoffmann, A. Balatsky, and S. Bonetti, Terahertz electric-field driven dynamical multiferroicity in $SrTiO_3$. Preprint at https://arxiv.org/abs/2210.01690 (2022).

[30] Dominik M. Juraschek, Michael Fechner, Alexander V. Balatsky, and Nicola A. Spaldin, "Dynamical multiferroicity," Phys. Rev. Materials **1**, 014401 (2017).

[31] R. Matthias Geilhufe, Vladimir Juričić, Stefano Bonetti, Jian-Xin Zhu, and Alexander V. Balatsky, "Dynamically induced magnetism in $KTaO_3$," Phys. Rev. Research **3**, L022011 (2021).

[32] R. Matthias Geilhufe and Wolfram Hergert, Electron magnetic moment of chiral phonons.

Preprint at https://arxiv.org/abs/2208.05746 (2022).

[33] Changjiang Liu, Xianjing Zhou, Deshun Hong, Brandon Fisher, Hong Zheng, John Pearson, Dafei Jin, Michael R Norman, and Anand Bhattacharya, arXiv:2203.05867 (2022).

[34] M. Sheik-Bahae, D. J. Hagan, and E. W. Van Stryland, "Dispersion and band-gap scaling of the electronic kerr effect in solids associated with two-photon absorption," Phys. Rev. Lett. **65**, 96–99 (1990).

[35] E. Jiménez, N. Mikuszeit, J. L. F. Cuñado, P. Perna, J. Pedrosa, D. Maccariello, C. Rodrigo, M. A. Niño, A. Bollero, J. Camarero, and R. Miranda, "Vectorial kerr magnetometer for simultaneous and quantitative measurements of the in-plane magnetization components," Review of Scientific Instruments **85**, 053904 (2014), https://doi.org/10.1063/1.4871098.

[36] M. Udina, T. Cea, and L. Benfatto, "Theory of coherent-oscillations generation in terahertz pump-probe spectroscopy: From phonons to electronic collective modes," Phys. Rev. B **100**, 165131 (2019).

[37] Lucas Huber, Sebastian F. Maehrlein, Feifan Wang, Yufeng Liu, and X.-Y. Zhu, "The ultrafast kerr effect in anisotropic and dispersive media," The Journal of Chemical Physics **154**, 094202 (2021), https://doi.org/10.1063/5.0037142.

[38] M. J. Weber, *Handbook of Optical Materials (1st ed.)* (CRC Press, 2002).

[39] S. V. Popov, Yu. P. Svirko, and N. I. Zheludev, "Pump-probe reflective polarization-sensitive nonlinear optics," Journal of the Optical Society of America B **13**, 2729 (1996).

[40] A. R. Bungay, S. V. Popov, N. I. Zheludev, and Yu. P. Svirko, "Specular nonlinear anisotropic polarization effect along fourfold crystal symmetry axes," Opt. Lett. **20**, 356–358 (1995).

[41] Yasusada Yamada and Gen Shirane, "Neutron scattering and nature of the soft optical phonon in $SrTiO_3$," Journal of the Physical Society of Japan **26**, 396–403 (1969), https://doi.org/10.1143/JPSJ.26.396.

[42] Giovanni Caldarelli, Michele Simoncelli, Nicola Marzari, Francesco Mauri, and Lara Benfatto, "Many-body green's function approach to lattice thermal transport," Phys. Rev. B **106**, 024312 (2022).

[43] F. Gabriele, M. Udina, and L. Benfatto, "Non-linear terahertz driving of plasma waves in layered cuprates," Nature Communications **12**, 752 (2021).

[44] Sebastian F. Maehrlein, Prakriti P. Joshi, Lucas Huber, Feifan Wang, Marie Cherasse, Yufeng Liu, Dominik M. Juraschek, Edoardo Mosconi, Daniele Meggiolaro, Filippo De Angelis,

and X.-Y. Zhu, "Decoding ultrafast polarization responses in lead halide perovskites by the two-dimensional optical kerr effect," Proceedings of the National Academy of Sciences **118**, e2022268118 (2021), https://www.pnas.org/doi/pdf/10.1073/pnas.2022268118.

[45] Maria N. Gastiasoro, Maria Eleonora Temperini, Paolo Barone, and Jose Lorenzana, "Theory of superconductivity mediated by rashba coupling in incipient ferroelectrics," Phys. Rev. B **105**, 224503 (2022).

# Supplementary Information

## ELECTRO-OPTIC CHARACTERIZATION OF THZ PUMP PULSES

The characterization of THz pump pulses has been performed using a 50 $\mu$m-thick GaP crystal cut along the [110] crystallographic direction and placed at the sample position. Multiple THz reflections inside GaP can be observed starting from $t \sim 0.5$ ps in Fig. S1(a). Nonetheless, this has no influence on the measurements shown in the main text, since the large absorption at THz frequencies in STO suppresses multiple reflections below the experimental noise level. Therefore, we considered the cut trace (up to $t \simeq 0.5$ ps) to simulate $\Delta\Gamma$ in the $t_{pp}$ time-domain. For comparison, Fig. S1(b) shows the $\bar{E}_{p,S}$ and $\bar{E}_{p,P}$ orthogonal components of the circular pump pulse, obtained by placing a THz quarter-wave plate after the band-pass filter.

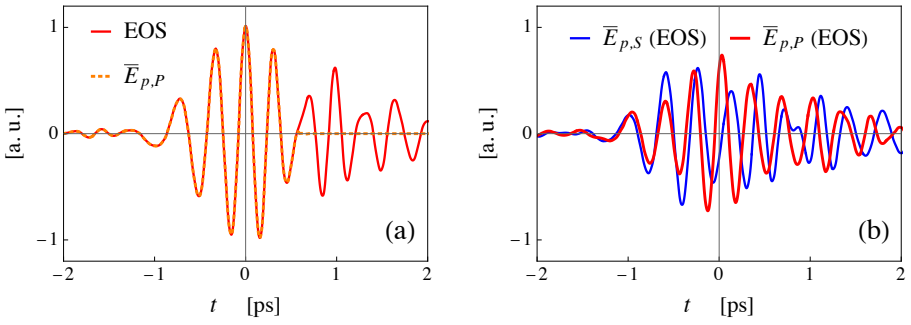


Figure S1. (a) Electro-optical sampling (EOS) of the linearly polarized terahertz field normalized to its maximum value (red plain line) and the cut time trace used in the simulation (dashed orange line). The maximum field amplitude is 330 kV/cm and the central frequency is $\emptyset_p/2\pi = 3$ THz. (b) Electro-optical sampling of the $\bar{E}_{p,S}$ (blue line) and $\bar{E}_{p,P}$ (red line) orthogonal components of the circularly polarized THz pulse, normalized as in (a). Here the maximum field amplitude is 230kV/cm, with central frequencies $\emptyset_{p,P(S)}/2\pi \simeq 3.1(2.9)$ THz.

## PUMP-PROBE POLARIZATION MISALIGNMENT

As mentioned in the main text, small deviations from the expected four-fold symmetric periodicity with zero average predicted by Eq. (6) are observed in the experimental data

(see Fig. 3**a**). In particular, when linearly polarized pump pulses are applied, the signal presents an overall positive (in the $SP$ configuration) or negative (in the $SS$ configuration) vertical shift. This slight deviation can be explained accounting for a small polarization misalignment $\Delta_\theta$ between the pump and the probe pulses with respect to the $S$ direction. More specifically, the pump pulse $\mathbf{E}_p(t)$ can be rewritten as

$$\mathbf{E}_p(t) = \begin{pmatrix} E_{p,S}(t)\sin(\theta+\Delta_\theta) + E_{p,P}(t)\cos(\theta+\Delta_\theta) \\ E_{p,S}(t)\cos(\theta+\Delta_\theta) - E_{p,P}(t)\sin(\theta+\Delta_\theta) \end{pmatrix}, \tag{S1}$$

while the probe field still forms an angle $\theta$ with respect to $y$ direction. Following the same steps detailed in the main text, the measured quantity $\Delta\Gamma$ at fixed $t^*_{pp}$ in the $SS$ linear configuration becomes

$$\Delta\Gamma^e(t^*_{pp},\theta,\Delta_\theta) \propto \bar{E}^2_{p,S}(t^*_{pp})\left[-(\chi^{(3)}_{xxxx}-3\chi^{(3)}_{xxyy})\sin(4\theta+2\Delta_\theta) + (\chi^{(3)}_{xxxx}+\chi^{(3)}_{xxyy})\sin(2\Delta_\theta)\right], \tag{S2}$$

where the second term accounts for the additional isotropic contribution leading to the observed negative shift of the signal when $\Delta_\theta < 0$. Such an explanation implies that the ratio between the overall constant shift and the maximum amplitude of the oscillating component should not depend on the spectral features of the pump pulse. This has been experimentally verified by slightly changing the alignment of incoming light in the $SS$ configuration, without filtering the broad-band THz pulse with the band-pass filter. The resulting vertical shift is consistent with the one observed in Fig. 3**a**, where instead narrow-band THz pulses were used.

## EXPLICIT DERIVATION OF PHONON-MEDIATED CONTRIBUTIONS

Here we explicitly show how each contribution to Eq. (10) can be associated with a third-order polarization sharing the same general structure of Eq. (5), i.e. linear with respect to the probe field and quadratic with respect to the pump. From a diagrammatic perspective (see Fig. S3), off-resonant interband electronic transitions leading to the EKE are associated with the bare electronic contribution $P^e$, coming from process (i), while the intermediate resonant excitation of the IR-active soft-phonon mode, responsible for the IKE, leads to the phonon-mediated contributions $P^{ph,(a)}$ and $P^{ph,(b)}$, associated with process (ii) and (iii) respectively. Each term can be obtained in a straightforward way by means of the effective-

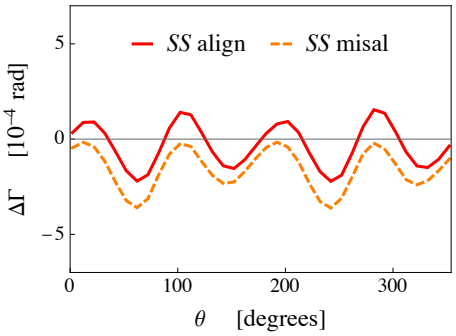


Figure S2. Experimental data as a function of $\theta$ at fixed time-delay $t^*_{pp}$, obtained using broad-band THz pulses. When the pump pulse is aligned along $S$ direction (plain red line) the signal oscillates around zero. If one introduces a small polarization misaligned with respect to $S$ direction (here we set $\Delta_\theta \simeq -6^\circ$), instead, an overall vertical shift is observed (dashed orange line), in agreement with Eq. (S2).

action approach, following the same steps detailed, e.g., in Ref.[36] for Raman-active phonon excitations in wide-band insulators.

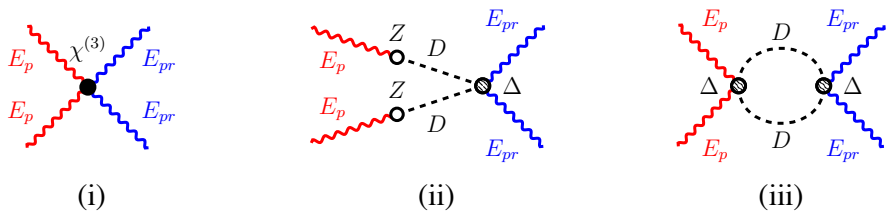


Figure S3. Diagrammatic representation of the fourth-order contributions to the effective-action $S[E]$, associated with (i) off-resonant electronic transitions and (ii)-(iii) phonon-mediated resonant excitations. Red (blue) wavy lines represents the pump (probe) field, black dashed lines the phonon propagator. The filled dot represents the nonlinear electron susceptibility $\chi^{(3)}$, empty dots the phonon effective charge $Z$ and dashed dots the two-phonon effective coupling $\Delta$.

In particular, the off-resonant electronic contribution $P^e$ can be related with the following action $S^e$ (see Fig. S3(i)), at fourth-order with respect to the external electromagnetic field $E$:

$$S^e[E] \sim \sum_{ijkl} \int E_{pr,i}(t) E_{pr,j}(t) \chi^{(3)}_{ijkl}(t-t') E_{p,k}(t') E_{p,l}(t') dt dt', \tag{S3}$$

which leads to the general Eq. (5) once the partial derivative with respect to the probe field has been performed, i.e. $P^e_i \equiv \partial S^e[E]/\partial E_{pr,i}$. When off-resonant (electronic) transitions

are considered $\chi^{(3)}_{ijkl}(t) \sim \chi^{(3)}_{ijkl}\delta(t)$. It is then useful to express the effective-action in the frequency domain, where the third-order susceptibility tensor is well approximated with the constant value $\chi^{(3)}_{ijkl}$. By performing the Fourier transform of each term, one then finds

$$S^e[E] \sim \sum_{ijkl} \chi^{(3)}_{ijkl} \int E_{p,l}(\emptyset_1) E_{p,k}(\emptyset_2) E_{pr,j}(\emptyset_3) E_{pr,i}(-\emptyset_1 - \emptyset_2 - \emptyset_3) d\emptyset_1 d\emptyset_2 d\emptyset_3, \tag{S4}$$

where $\emptyset_{1,2}(\emptyset_3)$ are generic incoming THz(eV) frequencies taken from the pump(probe) pulse.

Focusing now on phonon-mediated processes, in the first case (Fig. S3(ii)) two photons from the pump pulse linearly couple to the IR-active phonon mode before reaching the virtual electronic state, leading to the following contribution to the effective-action:

$$\begin{aligned} S^{ph,(a)}[E] \sim & \sum_{ijkl} \int E_{p,l}(\emptyset_1) Z_l D(\emptyset_1) E_{p,k}(\emptyset_2) Z_k D(\emptyset_2) \Delta_{lkij} \times \\ & \times E_{pr,j}(\emptyset_3) E_{pr,i}(-\emptyset_1 - \emptyset_2 - \emptyset_3) d\emptyset_1 d\emptyset_2 d\emptyset_3. \end{aligned} \tag{S5}$$

Here $D(\emptyset) \equiv \o_T/[(\Omega + i\gamma_T)^2 - \omega_T^2]$ is the phonon propagator in the frequency domain, $Z$ is related to the phonon effective charge and $\Delta$ gives the effective coupling between the two phonons and the (squared) probe field. Regardless of the specific temperature and frequency dependence of $Z$ and $\Delta$ coefficients, whose detailed evaluation goes beyond the scope of this work, notice that process (ii) should have in general the same polarization dependence of the bare electronic contribution (i), since $\delta\chi^{(a)}_{ijkl} \equiv Z_l Z_k \Delta_{lkij}$ shares in principle the same tensor structure of $\chi^{(3)}_{ijkl}$. By then introducing the effective force $F^{ph,(a)}_i(\emptyset) \equiv E_{p,i}(\emptyset) D(\emptyset)$, Eq. (S5) can be rewritten as

$$S^{ph,(a)}[E] \sim \sum_{ijkl} \delta\chi^{(a)}_{ijkl} \int F^{(a)}_l(\emptyset_1) F^{(a)}_k(\emptyset - \emptyset_1) E_{pr,j}(\emptyset_3) E_{pr,i}(-\emptyset - \emptyset_3) d\emptyset_1 d\emptyset d\emptyset_3, \tag{S6}$$

with $\emptyset = \emptyset_1 + \emptyset_2$, and the resulting third-order polarization in the time domain reads

$$P^{ph,(a)}_i(t, t_{pp}) \sim \sum_{jkl} \delta\chi^{(a)}_{ijkl} E_{pr,j}(t) \bar{F}^{(a)}_k(t + t_{pp}) \bar{F}^{(a)}_l(t + t_{pp}), \tag{S7}$$

where $\bar{F}^{(a)}_i(t) = \int dt' \bar{E}_{p,i}(t - t') D(t')$, being $\bar{E}_{p,i}(t)$ centered at $t = 0$.

In the second case, instead, the squared pump field first excites the (virtual) electronic state, which subsequently decays in two IR-active phonons (Fig. S3(iii)). Therefore, the effective coupling $\Delta$ describes both the interaction with the pump and with the probe pulses, and the resulting fourth-order contribution to the effective-action scales as $\delta\chi^{(b)}_{ijkl} \equiv \Delta_{ijkl}\Delta_{ijkl}$.

In the frequency domain, one then finds

$$S^{ph,(a)}[E] \sim \sum_{ijkl} \delta\chi^{(b)}_{ijkl} \int E_{p,l}(\emptyset_1) E_{p,k}(\emptyset_2) P(\emptyset_1 + \emptyset_2) \times \\ \times E_{pr,j}(\emptyset_3) E_{pr,i}(-\emptyset_1 - \emptyset_2 - \emptyset_3) d\emptyset_1 d\emptyset_2 d\emptyset_3, \tag{S8}$$

where $P(\emptyset)$ is the effective two-phonon propagator[43], i.e.

$$P(\emptyset) \sim \coth\left(\frac{\hbar\omega_T}{2k_B T}\right) \frac{\emptyset_T}{(\Omega + i0^+)^2 - 4\omega_T^2}, \tag{S9}$$

where we neglect the phonon dispersion for simplicity. One then replaces $i0^+ \rightarrow i2\gamma_T$ to account for the finite phonon life-time. Both the effective broadening $2\gamma_T$ and the coth term, accounting for the thermal distribution of the phonon population, can be explicitly obtained by deriving $P(\emptyset)$ at finite temperature $T$ using Matsubara formalism[42]. Going back to Eq. (S8), the corresponding third-order polarization in the time-domain reads

$$P_i^{ph,(b)}(t, t_{pp}) \sim \sum_{jkl} \delta\chi^{(b)}_{ijkl} E_{pr,j}(t) \int dt' P(t + t_{pp} - t') \bar{E}_{p,k}(t') \bar{E}_{p,l}(t'). \tag{S10}$$

Starting from Eq. (S7) and Eq. (S10), one then follows the same steps leading to Eq. (6) in the main text in order to derive $\Delta\Gamma^{ph,(a)}$ and $\Delta\Gamma^{ph,(b)}$ respectively. Notice that, while $\Delta\Gamma^{e}$ strictly follows the squared pump field in time, $\Delta\Gamma^{ph,(a)}$ follows the squared convolution between the pump and the phonon propagator (see Eq. (S7)), while $\Delta\Gamma^{ph,(b)}$ follows the convolution between the two-phonon propagator and the squared pump field (see Eq. (S10)). Due to the intermediate excitation of the phonon modes, each term shows a different phase factor in the time domain (see Fig. S4). Consequently, their combination leads to interference effects responsible for the temperature-dependent background signal observed in the experiments, in addition to the oscillating component at $\sim 2\Omega_p$.

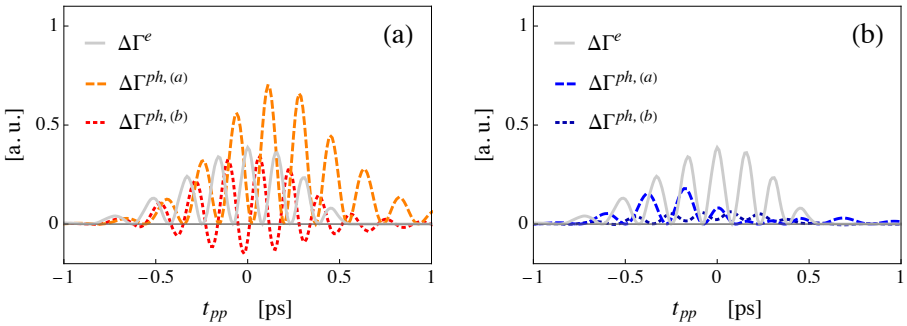


Figure S4. Simulated single contributions to $\Delta\Gamma(t_{pp})$ at 300 K (panel (a)) and 150 K (panel (b)). While the off-resonant electronic contribution $\Delta\Gamma^{e}$ (plain gray line) is expected to be temperature independent, the phonon mediated processes $\Delta\Gamma^{ph,(a)}$ (dashed lines) and $\Delta\Gamma^{ph,(a)}$ (dotted lines) are strongly suppressed at 150 K, when the resonant condition between the phonon propagator and the pump spectrum is lost (see Fig. 4**d**).